

Stabilization and operation of a Kerr-cat qubit

<https://doi.org/10.1038/s41586-020-2587-z>

Received: 28 July 2019

Accepted: 20 May 2020

Published online: 12 August 2020

 Check for updates

A. Grimm^{1,4,6}✉, N. E. Frattini^{1,6}, S. Puri², S. O. Mundhada¹, S. Touzard¹, M. Mirrahimi³, S. M. Girvin², S. Shankar^{1,5} & M. H. Devoret¹✉

Quantum superpositions of macroscopically distinct classical states—so-called Schrödinger cat states—are a resource for quantum metrology, quantum communication and quantum computation. In particular, the superpositions of two opposite-phase coherent states in an oscillator encode a qubit protected against phase-flip errors^{1,2}. However, several challenges have to be overcome for this concept to become a practical way to encode and manipulate error-protected quantum information. The protection must be maintained by stabilizing these highly excited states and, at the same time, the system has to be compatible with fast gates on the encoded qubit and a quantum non-demolition readout of the encoded information. Here we experimentally demonstrate a method for the generation and stabilization of Schrödinger cat states based on the interplay between Kerr nonlinearity and single-mode squeezing^{1,3} in a superconducting microwave resonator⁴. We show an increase in the transverse relaxation time of the stabilized, error-protected qubit of more than one order of magnitude compared with the single-photon Fock-state encoding. We perform all single-qubit gate operations on timescales more than sixty times faster than the shortest coherence time and demonstrate single-shot readout of the protected qubit under stabilization. Our results showcase the combination of fast quantum control and robustness against errors, which is intrinsic to stabilized macroscopic states, as well as the potential of these states as resources in quantum information processing^{5–8}.

A quantum system that can be manipulated and measured tends to interact with uncontrolled degrees of freedom in its environment, leading to decoherence. This presents a challenge to the experimental investigation of quantum effects and in particular to the field of quantum computing, where quantum bits (qubits) must remain coherent while operations are performed. Most noisy environments are only locally correlated and thus cannot decohere quantum information encoded in a non-local manner. Therefore, quantum information can be protected through the use of spatial distance^{9–11} or entangled qubit states^{12,13}. Crucially, this concept can be extended to non-local states in the phase space of a single oscillator^{2,14}, with the additional benefit of involving fewer physical components, a property termed hardware efficiency. The latter is desirable because fully protecting a quantum system against all forms of decoherence is likely to involve several layers of encodings, and it is crucial to introduce efficient error protection into the physical layer while maintaining simplicity^{6,7,15}.

A natural choice for non-locally encoding a qubit into the phase space of an oscillator is superpositions of macroscopically distinct coherent states—the so-called Schrödinger cat states. Here we choose the states $|C_{\alpha}^{\pm}\rangle = (|+\alpha\rangle \pm |-\alpha\rangle)/\sqrt{2}$ with average photon number $\bar{n} = |\alpha|^2$ and, respectively, even and odd photon number parity as the Z eigenstates of the encoded qubit (Fig. 1a). The coherent states $|+\alpha\rangle$ and $|-\alpha\rangle$ are

the approximate X eigenstates (Supplementary Information section I), and their distance in phase space ensures protection against any noise process that causes local displacements in this space. Crucially, this leads to a suppression of phase flips that is exponential in the average photon number \bar{n} (refs. ^{1,2}). In particular, photon loss, the usual noise process in an oscillator, cannot induce transitions between $|+\alpha\rangle$ and $|-\alpha\rangle$ because they are eigenstates of the annihilation operator \hat{a} . This is not the case for their superpositions, so a stochastic photon-loss event corresponds to a bit-flip error on the encoded qubit: $\hat{a}|C_{\alpha}^{\pm}\rangle = \alpha|C_{\alpha}^{\mp}\rangle$, which also affects the parity-less Y eigenstates $|C_{\alpha}^{\mp i}\rangle = (|+\alpha\rangle \mp i|-\alpha\rangle)/\sqrt{2}$, where $i = \sqrt{-1}$. However, for a given single-photon-loss rate κ_a , the bit-flip rate of approximately $2\bar{n}\kappa_a$ (ref. ¹⁶, Supplementary Information section XI) increases only linearly with the photon number. A qubit with such ‘biased noise’ is an important resource in fault-tolerant quantum computation^{17,18}. Additional layers of error correction can then focus strongly on the remaining bit-flip error^{6,7,18}. This substantially reduces the hardware complexity compared with conventional approaches that use qubits without such error protection.

Here we show that such a protected qubit can be stabilized autonomously in a simple and versatile implementation similar to a superconducting transmon under parametric driving. Unlike in other hardware-efficient encodings^{19–21}, the most nonlinear mode of our

¹Department of Applied Physics, Yale University, New Haven, CT, USA. ²Department of Physics, Yale University, New Haven, CT, USA. ³QUANTIC team, Inria Paris, Paris, France. ⁴Present address: Photon Science Division, Paul Scherrer Institut, Villigen, Switzerland. ⁵Present address: Electrical and Computer Engineering, University of Texas, Austin, TX, USA. ⁶These authors contributed equally: A. Grimm, N. E. Frattini. ✉e-mail: alexander.grimm@psi.ch; michel.devoret@yale.edu

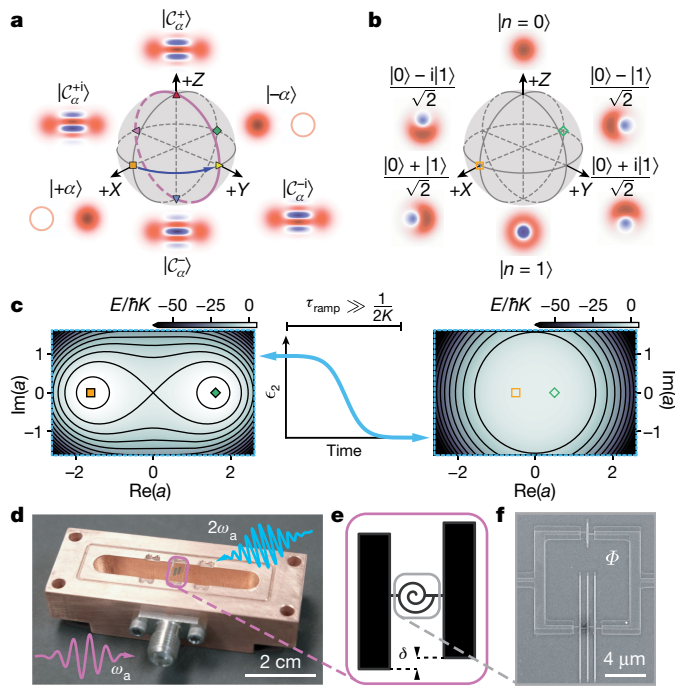


Fig. 1 | Qubit encoding, stabilization and implementation. **a**, Bloch sphere of the protected Kerr-cat qubit (KCQ) in the large- α limit (Supplementary Information section I). The states on all six cardinal points are labelled, indicated by coloured markers, and their Wigner function¹⁶ phase-space representations are sketched. Here, $|\pm Z\rangle = |C_\alpha^\pm\rangle = (|\alpha\rangle \pm |-\alpha\rangle)/\sqrt{2}$ and $|\pm Y\rangle = |C_\alpha^\pm i\rangle = (|\alpha\rangle \mp i|-\alpha\rangle)/\sqrt{2}$. The continuous $X(\theta)$ gate with the arbitrary rotation angle θ and the discrete $Z(\pi/2)$ gate are shown by a purple circle and a blue arrow, respectively. **b**, Bloch sphere of the single-photon Fock qubit (FQ). **c**, Energy (E) dependence of equation (1) on classical phase-space coordinates $\text{Re}(a)$ and $\text{Im}(a)$ for squeezing drive amplitudes $\epsilon_2/2\pi = 17.75$ MHz (left) and $\epsilon_2 = 0$ (right) with a sketch showing the adiabatic ramp of the drive over a time $\tau_{\text{ramp}} \gg 1/2K$. Black lines are constant energy contours. The quadrature expectation values of the $|\pm X\rangle$ states from **a**, **b** are indicated by their respective markers. **d**, Photograph of the nonlinear resonator (purple frame) inside the copper section of the readout cavity (Methods). Also represented are the $X(\theta)$ -rotation drive (ω_s) and the squeezing-generation drive ($2\omega_s$). **e**, Schematic of the nonlinear resonator with pad offset δ to set the dispersive coupling to the readout cavity (Methods) and spiral symbol representing the nonlinear inductor (SNAIL element). **f**, Scanning electron micrograph of the SNAIL element consisting of four Josephson junctions in a loop threaded by an external magnetic flux ϕ .

system encodes and stabilizes the qubit without requiring auxiliary nonlinear modes that could introduce additional uncorrectable errors.

For this protected qubit to be practical, it is essential that operations can be performed faster than the shortest decoherence timescale, here the bit-flip time. We experimentally demonstrate such fast gate operations and quantum non-demolition single-shot readout in a system that maintains phase-flip protection via the simultaneous stabilization of two opposite-phase coherent states.

Our approach is based on the application of a resonant single-mode squeezing drive to a Kerr-nonlinear resonator⁴. In the frame rotating at the resonator frequency ω_a , the system is described by the Hamiltonian

$$\hat{H}_{\text{cat}}/\hbar = -K\hat{a}^{\dagger 2}\hat{a}^2 + \epsilon_2(\hat{a}^{\dagger 2} + \hat{a}^2), \quad (1)$$

where K is the Kerr nonlinearity, ϵ_2 is the amplitude of the squeezing drive and \hbar is the reduced Planck's constant. Some intuition on this system can be gained from computing $\langle \hat{H}_{\text{cat}} \rangle$ as a function of classically treated phase-space coordinates. There are two stable extrema at $\pm\alpha = \pm\sqrt{\epsilon_2/K}$, as indicated by the markers in Fig. 1c. They correspond to the lowest degenerate eigenstates of the quantum Hamiltonian⁴ (Supplementary Information) and thus do not decay to vacuum.

These eigenstates are separated from the rest of the spectrum by an energy gap $E_{\text{gap}}/\hbar \approx 4K\bar{n}$ (Supplementary Information section III, Supplementary Fig. 1), which sets the speed limit for operations and readout. The energy barrier between these eigenstates prevents jumps along the X -axis of this ‘Kerr-cat qubit’ (KCQ). If no squeezing drive is applied, \hat{H}_{cat} reduces to the Hamiltonian of an anharmonic oscillator. This resembles a superconducting transmon with anharmonicity $2K$, commonly used to encode a ‘Fock qubit’ (FQ) into the first two photon number states $|0\rangle$ and $|1\rangle$ (Fig. 1b). Its classical energy displays one single extremum in phase space harbouring the quadrature expectation values of both X eigenstates without the protection of an energy barrier (Fig. 1c, right panel). By toggling the squeezing drive, a Kerr-nonlinear resonator can be tuned to implement either type of qubit.

Our experimental implementation consists of a superconducting nonlinear resonator placed inside a three-dimensional (3D) microwave cavity (Fig. 1d). This is a standard setup in 3D transmon qubits with a few key modifications (Methods). The foremost modification, employing a superconducting nonlinear asymmetric inductive element (SNAIL)²² as a nonlinear inductor (Fig. 1f), allows us to create single-mode squeezing by applying a coherent microwave drive ω_s at twice the resonator frequency ω_a and makes the resonator flux tunable. Here we tune our device to a frequency $\omega_a/2\pi = 6$ GHz and Kerr nonlinearity $K/2\pi = 6.7$ MHz. At this frequency, the FQ has an amplitude damping time $T_1 = 15.5$ μs and a transverse relaxation time $T_2 = 3.4$ μs .

The FQ is employed for initialization and measurement of the KCQ during most experiments described in this work. This is possible because the states $|0\rangle$, $|C_\alpha^+\rangle$ ($|1\rangle$, $|C_\alpha^-\rangle$) spanning the two Bloch spheres have the same even (odd) photon number parity, which is conserved by the system Hamiltonian (equation (1)). Consequently, ramping the squeezing drive on and off slowly with respect to $1/2K$, as sketched in Fig. 1c, adiabatically maps between the FQ and KCQ (Methods).

We now show that we indeed implement the Hamiltonian (1), and thus initialize and stabilize a KCQ, by demonstrating the unique features of Rabi oscillations around the X axis of its Bloch sphere. To this end, we apply an additional coherent drive $\epsilon_x\hat{a}^{\dagger} + \epsilon_x^*\hat{a}$ with amplitude ϵ_x and frequency $\omega_a = \omega_s/2$ to the system. This lifts the degeneracy between the states $|\alpha\rangle$ and $|-\alpha\rangle$, and therefore leads to oscillations with a Rabi frequency

$$\Omega_x = \text{Re}(4\epsilon_x\alpha) \quad (2)$$

between their superposition states along the purple circle in Fig. 1a. This picture is valid for large enough α and for $\epsilon_x \ll E_{\text{gap}}/\hbar$ (ref. 4; see also Supplementary Information section IV). Note that equation (2) is different from the Rabi frequency of a FQ in two ways. First, it depends on the amplitude of the squeezing drive through $\alpha \propto \sqrt{\epsilon_2}$. Second, it varies with the phase of the applied Rabi drive $\arg(\epsilon_x)$ (for simplicity we chose $\epsilon_2, \alpha \in \mathbb{R}$).

We first focus on the effect of the squeezing drive on the Rabi frequency. We initialize in $|C_\alpha^+\rangle$ and apply a Rabi drive with constant $|\epsilon_x|$ and $\arg(\epsilon_x) = 0$ for a variable time Δt and a variable amplitude ϵ_2 (Fig. 2a). Figure 2b shows the Rabi frequencies for each ϵ_2 , extracted from the oscillations in the measured FQ $|0\rangle$ -state population fraction at the end of the experiment. For $\epsilon_2 = 0$, we are simply driving FQ Rabi oscillations giving a direct calibration of $|\epsilon_x|/2\pi = 740$ kHz. For large values of ϵ_2 , the Rabi frequency becomes a linear function of $\sqrt{\epsilon_2}$, confirming the theoretical prediction of equation (2). The solid black line shows a one-parameter fit to a numerical simulation of our experiment (Methods).

We now turn to another unique feature of these Rabi oscillations by setting $\epsilon_2/2\pi = 15.5$ MHz and varying Δt and $\arg(\epsilon_x)$. As expected, the measured oscillations shown in Fig. 2c are π -periodic in $\arg(\epsilon_x)$. Three cuts through this data (dashed lines) are shown in Fig. 2d. The top panel

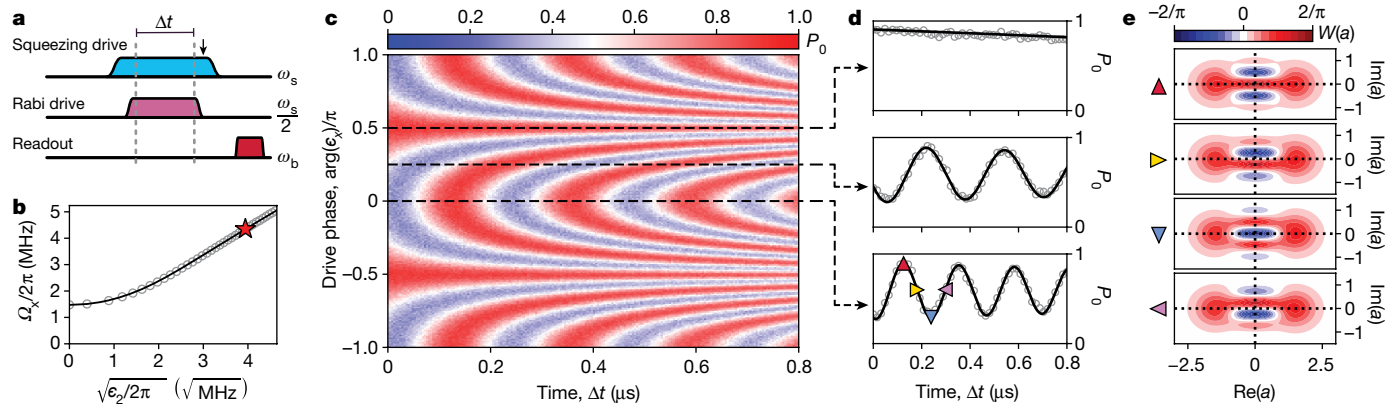


Fig. 2 | Rabi oscillations of the protected KCQ. **a**, Pulse sequence to perform the following functions: (1) initialize the KCQ ($|0\rangle \rightarrow |C_a^+\rangle$), (2) drive Rabi oscillations for a varying time Δt , and (3) map onto the FQ and perform dispersive readout. ω_s , $\omega_s/2$ and ω_b are the frequencies of the respective drives. A black arrow indicates the endpoint of the numerical simulations performed for **b**, **d**, **e** (Methods). **b**, Dependence of the Rabi frequency Ω_x on $\sqrt{\epsilon_2}$. Experimental data are open grey circles. The solid black line is a one-parameter fit to the data used to calibrate ϵ_2 (Methods). The red star indicates the condition $\epsilon_2/2\pi = 15.5$ MHz used for **c**, **d**, **e**. **c**, Dependence of the experimentally measured Rabi oscillations on time Δt and on the phase of the Rabi drive $\arg(\epsilon_x)$.

The colour scale gives the ground state population of the FQ (P_0) at the end of the experiment. **d**, Cuts of **c** for the three Rabi-drive phases indicated by dashed lines. Open grey circles are the experimental data and black lines are the simulation. Symbols in the bottom panel indicate the times for which the simulated oscillator state is shown in **e**. **e**, Simulated phase-space representation of the oscillator density matrix corresponding to the $|+Z\rangle$, $|+Y\rangle$, $|-Z\rangle$ and $|-Y\rangle$ states of the KCQ (from top to bottom). The colour scale gives the value of the Wigner function $W(a)$ as a function of the real and imaginary part of the phase-space coordinate a .

corresponds to a phase difference of $\pi/2$ between the coherent state amplitude and the Rabi drive, meaning that oscillations are suppressed. The middle and bottom panels at respective phase differences of $\pi/4$ and 0 display increasing Rabi frequencies, with the latter corresponding to the red star marker in Fig. 2b. In the bottom panel, the black line is the result of a numerical simulation scaled to match the contrast of the data. The black lines in the top and middle panels use the same scaling factor and are thus parameter-free predictions in good agreement with the measured data. Having benchmarked our simulation in this way, we use it to compute the full density matrix of the resonator, which we represent with Wigner functions (Fig. 2e). Apart from slight asymmetries due to the finite ramp time of the initial mapping pulse, they agree well with the expected $|+Z\rangle$, $|+Y\rangle$, $|-Z\rangle$ and $|-Y\rangle$ states of the KCQ.

Next, we characterize the mapping operation and a set of single-qubit gates on the KCQ by performing process tomography (Methods). In all subsequent experiments, the average photon number of the cat states is set to $\bar{n} \approx 2.6$ and frequency shifts induced by the squeezing drive are taken into account by setting $\omega_s/2 = \tilde{\omega}_a$, where $\tilde{\omega}_a$ is the Stark-shifted resonator frequency (Supplementary Information section II). The pulse sequence for tomography of the mapping between the FQ and the KCQ is shown in Fig. 3a and the measured state vectors are plotted on a Bloch sphere in Fig. 3b. An estimate of the fidelity $\mathcal{F}_{\text{map}} \approx 0.855 \pm 0.002$ (\pm one standard deviation here and for all subsequent values) is obtained by using the Pauli transfer matrix approach²³ (Supplementary Information). This number reflects the fidelity of the tomography FQ pulses as well as of the mapping itself, because, apart from a normalization by the FQ Rabi contrast, the presented fidelities include state-preparation-and-measurement (SPAM) errors (Supplementary Information section V). We expect these errors to be dominated by decoherence during the comparatively slow adiabatic ramps. This could be remedied in future experiments by using optimal pulse shapes, which can reduce the duration of the mapping operation by a factor of more than 40 with respect to its present value⁴.

We now turn to the pulse sequence shown in Fig. 3c, which additionally performs an $X(\pi/2)$ gate on the KCQ. The process tomography data (Fig. 3d) shows the desired rotation around the X -axis with a fidelity of $\mathcal{F}_{X(\pi/2)} \approx 0.857 \pm 0.001$. Comparing this value to \mathcal{F}_{map} indicates that $\mathcal{F}_{X(\pi/2)}$ is mostly limited by SPAM errors. From a complementary

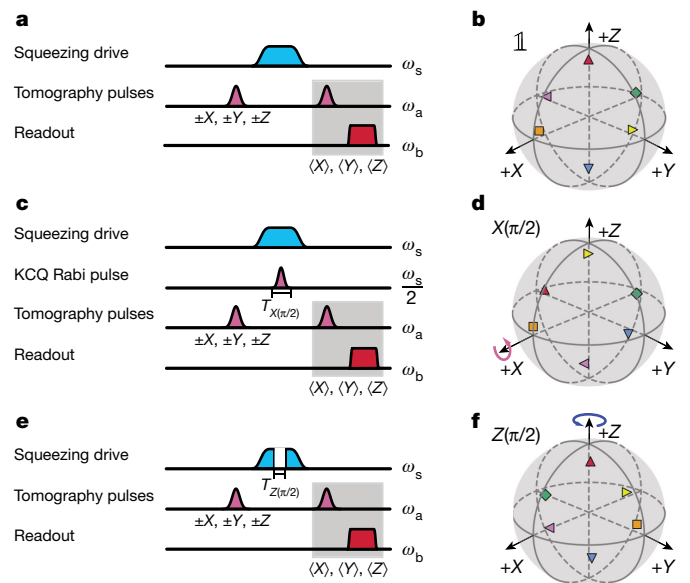


Fig. 3 | KCQ gate process tomography. **a**, **c**, **e**, Pulse sequences for process tomography of mapping between FQ and KCQ, which is ideally the identity operation $\mathbb{1}$ (**a**), mapping and the $X(\pi/2)$ gate (**c**), as well as mapping and the $Z(\pi/2)$ gate (**e**). In each sequence, the FQ is initialized on the $\pm X$, $\pm Y$ and $\pm Z$ cardinal points of the Bloch sphere, the respective operation is performed, and the expectation values $\langle X \rangle$, $\langle Y \rangle$ and $\langle Z \rangle$ are measured by a combination of FQ pulses and dispersive readout (grey box). In **c**, $T_{X(\pi/2)} = 24$ ns is the total duration of the Gaussian Rabi pulse applied to the KCQ. In **e**, $T_{Z(\pi/2)} = 38$ ns is the duration for which the squeezing drive is switched off to perform the gate. **b**, **d**, **f**, Process tomography results presented on a Bloch sphere for the operations $\mathbb{1}$ (**b**), $X(\pi/2)$ (**d**) and $Z(\pi/2)$ (**f**). The expectation-value vector after the operation for an initialization on the $(+X, -X, +Y, -Y, +Z, -Z)$ cardinal point is represented by an (orange square, green diamond, gold right-facing triangle, purple left-facing triangle, red upward-facing triangle, blue downward-facing triangle). Error bars are smaller than the size of the markers. The fidelities are 0.855 ± 0.002 , 0.857 ± 0.001 and 0.811 ± 0.001 , respectively.

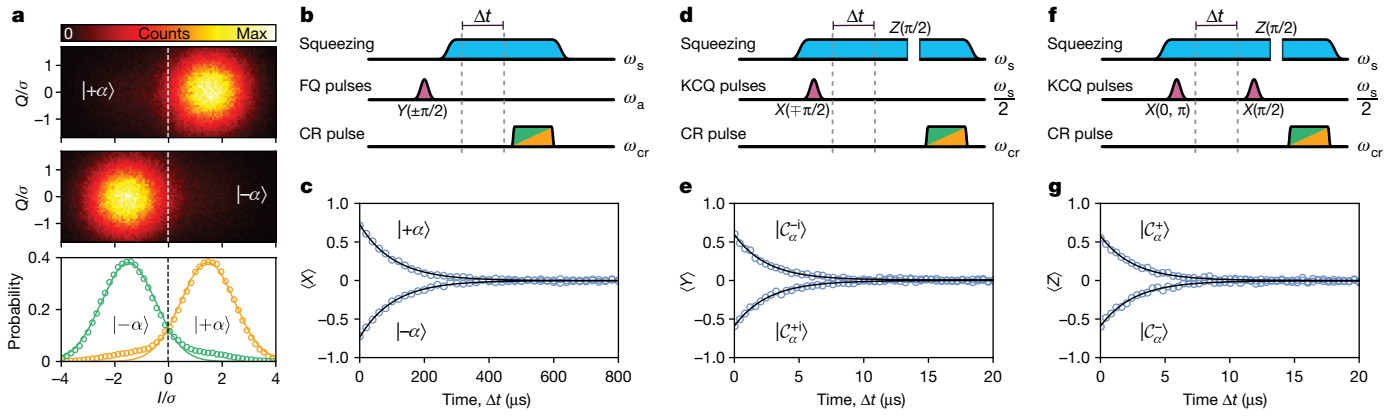


Fig. 4 | Cat-quadrature readout (CR) and coherence times. **a**, Top and middle: histogram of the cavity output field when performing CR (see **b**) after preparation of either $|+\alpha\rangle$ (top) or $|-\alpha\rangle$ (middle). Bottom: corresponding probability distribution along the I -quadrature. Open orange (green) circles show measured data for $|+\alpha\rangle$ ($|-\alpha\rangle$) and solid lines are Gaussian fits of width σ used to scale the quadrature axes, I and Q . Setting a threshold at $I/\sigma = 0$ (dashed line) implements a direct single-shot readout of the KCQ along its X -axis. **b**, CR pulse sequence for the measurements presented in **a**, **c**. After state initialization in $|\pm\alpha\rangle$ ($Y(\pm\pi/2)$ gate on the FQ and mapping), a pulse at frequency $\omega_{cr} = \omega_b - \omega_s/2$ is applied for a time $T_{cr} = 3.6 \mu\text{s}$ converting the quadrature amplitude of the KCQ to a drive on the readout cavity at ω_b . The wait time Δt is set to zero to obtain the results shown in **a**

and varied in **c**, KCQ $\langle X \rangle$ -component coherence. Open blue circles are data and solid black lines are single-exponential fits with decay times $\tau_{+x} = 105 \mu\text{s} \pm 1 \mu\text{s}$ and $\tau_{-x} = 106 \mu\text{s} \pm 1 \mu\text{s}$. **d**, Pulse sequence for **e**. After initialization in $|C_\alpha^{\pm}\rangle$ (mapping $|0\rangle \rightarrow |C_\alpha^{\pm}\rangle$ and $X(\mp\pi/2)$ gate) and variable wait time Δt , a $Z(\pi/2)$ gate is performed followed by CR. **e**, KCQ $\langle Y \rangle$ -component coherence. Open blue circles are data and solid black lines are single-exponential fits with decay times $\tau_{+y} = 2.51 \mu\text{s} \pm 0.06 \mu\text{s}$ and $\tau_{-y} = 2.60 \mu\text{s} \pm 0.05 \mu\text{s}$. **f**, Pulse sequence for **g**. After initialization in $|C_\alpha^{\pm}\rangle$ (mapping $|0\rangle \rightarrow |C_\alpha^{\pm}\rangle$ and either $X(0)$ or $X(\pi)$ gate) and variable wait time Δt , a $X(\pi/2)$ gate and a $Z(\pi/2)$ gate are performed followed by CR. **g**, KCQ $\langle Z \rangle$ -component coherence. Open blue circles are data and solid black lines are single-exponential fits with decay times $\tau_{+z} = 2.60 \mu\text{s} \pm 0.07 \mu\text{s}$ and $\tau_{-z} = 2.56 \mu\text{s} \pm 0.07 \mu\text{s}$.

measurement (Supplementary Fig. 3), we estimate the infidelity due to over-rotation and decoherence during the gate operation to about 0.01. As this operation is compatible with an arbitrary angle of rotation, only a $\pi/2$ rotation around the Z -axis is needed to reach any point on the KCQ Bloch sphere. Nominally, such a gate is incompatible with the stabilization as it could be used to go between the states $|+\alpha\rangle$ and $|-\alpha\rangle$. However, for $\epsilon_2 = 0$, the free evolution of the Kerr Hamiltonian for a time $\pi/2K \approx 37.3 \text{ ns}$ achieves the required operation^{4,24,25} (Methods and Fig. 3e). The tomography data shown in Fig. 3f gives a fidelity $\mathcal{F}_{Z(\pi/2)} \approx 0.811 \pm 0.001$. We attribute the reduction of fidelity with respect to \mathcal{F}_{map} to the difference between the actual gate time $T_{Z(\pi/2)} = 38 \text{ ns}$ and $\pi/2K$, and to the finite rise time of the step function in ϵ_2 of about 4 ns; both of which are not limitations of our device but of our room-temperature electronics (Supplementary Information section VI).

So far, we have characterized the basic properties and gate operations of the KCQ by mapping back onto the FQ and using the well-understood dispersive readout method. This readout, however, destroys the state of the KCQ. We now demonstrate an entirely new way to perform a quantum non-demolition measurement on the X component of the stabilized KCQ, which we call the ‘cat-quadrature readout’ (CR). We apply an additional drive at frequency $\omega_{cr} = \omega_b - \omega_s/2$, where ω_b is the frequency of the readout cavity. Through the three-wave mixing capability of our system, this generates a frequency-converting interaction between the nonlinear resonator and the readout cavity. In the frame rotating at both $\omega_s/2 = \tilde{\omega}_s$ and ω_b , this adds the following term to equation (1):

$$\hat{H}_{cr}/\hbar = ig_{cr}(\hat{a}\hat{b}^\dagger - \hat{a}^\dagger\hat{b}). \quad (3)$$

Here, \hat{b} is the annihilation operator of the cavity field and $g_{cr}/2\pi = 1.7 \text{ MHz}$ is the independently measured coupling strength (Supplementary Fig. 6). For a quadrature expectation value $(\hat{a} + \hat{a}^\dagger)/2 = \pm\alpha$ in the nonlinear resonator, this causes an effective coherent drive on the cavity and projects the KCQ onto the corresponding state $|\pm\alpha\rangle$ along its X -axis. We gain information about the result of this projection by measuring the emitted cavity field.

We characterize the fidelity of this readout by first initializing the KCQ along its X -axis and then applying a CR pulse for a time $T_{cr} = 3.6 \mu\text{s}$ as shown in Fig. 4b. Two histograms of the measured cavity field are shown in Fig. 4a for initialization in $|+\alpha\rangle$ and $|-\alpha\rangle$, respectively. Their separation is large enough to implement a single-shot readout by setting a threshold at $I/\sigma = 0$ with total fidelity $\mathcal{F} = 0.74$ (Methods), where I/σ is a dimensionless quantity corresponding to the I -quadrature signal divided by the standard deviation σ of the histograms. This fidelity is a lower bound including errors in state preparation caused by the thermal population of the FQ $|1\rangle$ state (contributing an infidelity of about $2 \times 4\% = 8\%$) and imperfections during the initial FQ pulse and mapping. Finally, we characterize the quantum-non-demolition aspect of the CR as $\mathcal{Q} = 0.85$ from two successive measurements (Methods).

We now use this CR to investigate the phase-flip time of the KCQ. The decay of the $\langle X \rangle$ component for either initial state along this axis is measured using the pulse sequence shown in Fig. 4b. We fit the data to a single-exponential decay with characteristic times $\tau_{+x} = 105 \mu\text{s} \pm 1 \mu\text{s}$ and $\tau_{-x} = 106 \mu\text{s} \pm 1 \mu\text{s}$. Additional measurements with dispersive readout confirm this result (Supplementary Fig. 7).

Similarly, the coherence times of both the $\langle Y \rangle$ and $\langle Z \rangle$ components are measured using CR, but employing only operations on the KCQ after the initial $|0\rangle \rightarrow |C_\alpha^{\pm}\rangle$ mapping operation (Fig. 4d, f). The resulting decay curves are displayed in Fig. 4e, g. Single-exponential fits of the data yield the decay times $\tau_{+y} = 2.51 \mu\text{s} \pm 0.06 \mu\text{s}$, $\tau_{-y} = 2.60 \mu\text{s} \pm 0.05 \mu\text{s}$, $\tau_{+z} = 2.60 \mu\text{s} \pm 0.07 \mu\text{s}$ and $\tau_{-z} = 2.56 \mu\text{s} \pm 0.07 \mu\text{s}$. These values are slightly smaller than the predicted bit-flip time due to photon loss $\tau_{\text{loss}} = T_1/2\tilde{n} = 2.98 \mu\text{s}$. We expect that photon-gain processes play a role in this reduction (Supplementary Information section XI, Supplementary Fig. 8).

Our results demonstrate a 30-fold increase in the phase-flip time of the protected KCQ with respect to the FQ. Crucially, we perform a full set of single-qubit gates on the protected qubit on timescales that are much shorter than its bit-flip time. Although the measured gate fidelities are limited by SPAM errors, an upper bound of the error rate due to decoherence during the gate operations is given by: $T_{X(\pi/2)}/\tau_{+y} \approx T_{Z(\pi/2)}/\tau_{+y} < 2 \times 10^{-2}$. The combination of error protection, fast gates and single-shot readout opens the door to using stabilized Schrödinger cat states as physical qubits in a future quantum computer.

The simplicity of our implementation provides a straightforward path to coupling several KCQs and demonstrating operations between them. In particular, our qubit permits a noise-bias-preserving controlled-NOT gate⁶, which would be impossible with standard two-level qubits⁷. Moreover, KCQs could be applied as auxiliary systems for fault-tolerant error detection on other logical qubits⁵. This will require further improvements in device performance such as the bit-flip time, currently limited by losses due to the copper cavity.

The limitation of the phase-flip time also requires further investigation. Measurements performed at other flux points with different strengths of the third- and fourth-order nonlinearities indicate that coherence decreases when stronger drives have to be applied to the system to reach similar photon numbers. Similarly, an increase in photon number beyond the $\tilde{n} \approx 2.6$ operating point chosen in this work decreases coherence. This is probably related to heating effects associated with the strong driving of Josephson junction devices^{26,27} causing leakage to higher excited states outside of the KCQ encoding. Such leakage can be counteracted through controlled two-photon dissipation back towards the states of the KCQ⁵. This dissipation-based approach to stabilization has been effective in achieving strongly biased noise²⁸, but quantum operations that are much faster than all coherence timescales of the encoded qubit remain difficult to achieve²⁹. The optimal solution should be to rely on a combination of two-photon dissipation, squeezing drive and Kerr nonlinearity for phase-flip suppression and on the Kerr nonlinearity for high gate speeds.

In addition to its applications in fault-tolerant quantum computation^{4–6,8}, our system extends the understanding of bistability in parametrically driven Kerr nonlinear oscillators from the classical regime^{30–33} to the quantum regime where nonlinearity dominates over losses^{24,25,34,35}. Our results demonstrate long-lived quantum superpositions of degenerate, macroscopically distinct semi-classical states arising from Hamiltonian bistability. Such states could shed light on the quantum-classical transition³⁶ and can be useful in weak force measurements³⁷. Networks of coupled bistable oscillators can be mapped onto Ising spins and used to investigate non-equilibrium quantum phase transitions³⁸ or to solve combinatorial optimization problems^{39–41}. These examples suggest that our Kerr-cat system is likely to be applied both to quantum computation and for the investigation of fundamental quantum effects.

Online content

Any methods, additional references, Nature Research reporting summaries, source data, extended data, supplementary information, acknowledgements, peer review information; details of author contributions and competing interests; and statements of data and code availability are available at <https://doi.org/10.1038/s41586-020-2587-z>.

1. Cochrane, P. T., Milburn, G. J. & Munro, W. J. Macroscopically distinct quantum-superposition states as a bosonic code for amplitude damping. *Phys. Rev. A* **59**, 2631–2634 (1999).
2. Mirrahimi, M. et al. Dynamically protected cat-qubits: a new paradigm for universal quantum computation. *New J. Phys.* **16**, 045014 (2014).
3. Milburn, G. J. & Holmes, C. A. Quantum coherence and classical chaos in a pulsed parametric oscillator with a Kerr nonlinearity. *Phys. Rev. A* **44**, 4704–4711 (1991).
4. Puri, S., Boutin, S. & Blais, A. Engineering the quantum states of light in a Kerr-nonlinear resonator by two-photon driving. *npj Quantum Inf.* **3**, 18 (2017).
5. Puri, S. et al. Stabilized cat in a driven nonlinear cavity: a fault-tolerant error syndrome detector. *Phys. Rev. X* **9**, 041009 (2019).
6. Puri, S. et al. Bias-preserving gates with stabilized cat qubits. *Sci. Adv.* (in the press); preprint at <https://arxiv.org/abs/1905.00450> (2019).

7. Guillaud, J. & Mirrahimi, M. Repetition cat qubits for fault-tolerant quantum computation. *Phys. Rev. X* **9**, 041053 (2019).
8. Goto, H. Universal quantum computation with a nonlinear oscillator network. *Phys. Rev. A* **93**, 050301 (2016).
9. Kitaev, A. Y. Fault-tolerant quantum computation by anyons. *Ann. Phys.* **303**, 2–30 (2003).
10. Oreg, Y., Refael, G. & von Oppen, F. Helical liquids and Majorana bound states in quantum wires. *Phys. Rev. Lett.* **105**, 177002 (2010).
11. Lutchyn, R. M., Sau, J. D. & Das Sarma, S. Majorana fermions and a topological phase transition in semiconductor–superconductor heterostructures. *Phys. Rev. Lett.* **105**, 077001 (2010).
12. Shor, P. W. Scheme for reducing decoherence in quantum computer memory. *Phys. Rev. A* **52**, R2493–R2496 (1995).
13. Fowler, A. G., Mariantoni, M., Martinis, J. M. & Cleland, A. N. Surface codes: towards practical large-scale quantum computation. *Phys. Rev. A* **86**, 032324 (2012).
14. Gottesman, D., Kitaev, A. & Preskill, J. Encoding a qubit in an oscillator. *Phys. Rev. A* **64**, 012310 (2001).
15. Vuillot, C., Asasi, H., Wang, Y., Pryadko, L. P. & Terhal, B. M. Quantum error correction with the toric Gottesman–Kitaev–Preskill code. *Phys. Rev. A* **99**, 032344 (2019).
16. Haroche, S. & Raimond, J.-M. *Exploring the Quantum: Atoms, Cavities and Photons* (Oxford Univ. Press, 2006).
17. Aliferis, P. & Preskill, J. Fault-tolerant quantum computation against biased noise. *Phys. Rev. A* **78**, 052331 (2008).
18. Tuckett, D. K., Bartlett, S. D. & Flammia, S. T. Ultrahigh error threshold for surface codes with biased noise. *Phys. Rev. Lett.* **120**, 050505 (2018).
19. Ofek, N. et al. Extending the lifetime of a quantum bit with error correction in superconducting circuits. *Nature* **536**, 441–445 (2016).
20. Hu, L. et al. Quantum error correction and universal gate set operation on a binomial bosonic logical qubit. *Nat. Phys.* **15**, 503–508 (2019).
21. Campagne-Ibarcq, P. et al. Quantum error correction of a qubit encoded in grid states of an oscillator. *Nature* <http://doi.org/10.1038/s41586-020-2603-3> (2020).
22. Frattini, N. E. et al. 3-wave mixing Josephson dipole element. *Appl. Phys. Lett.* **110**, 222603 (2017).
23. Chow, J. M. et al. Universal quantum gate set approaching fault-tolerant thresholds with superconducting qubits. *Phys. Rev. Lett.* **109**, 060501 (2012).
24. Yurke, B. & Stoler, D. The dynamic generation of Schrödinger cats and their detection. *Physica B+C* **151**, 298–301 (1988).
25. Kirchmair, G. et al. Observation of quantum state collapse and revival due to the single-photon Kerr effect. *Nature* **495**, 205–209 (2013).
26. Sank, D. et al. Measurement-induced state transitions in a superconducting qubit: beyond the rotating wave approximation. *Phys. Rev. Lett.* **117**, 190503 (2016).
27. Lescanne, R. et al. Escape of a driven quantum Josephson circuit into unconfined states. *Phys. Rev. Appl.* **11**, 014030 (2019).
28. Lescanne, R. et al. Exponential suppression of bit-flips in a qubit encoded in an oscillator. *Nat. Phys.* **16**, 509–513 (2020).
29. Touzard, S. et al. Coherent oscillations inside a quantum manifold stabilized by dissipation. *Phys. Rev. X* **8**, 021005 (2018).
30. Dykman, M. I., Maloney, C. M., Smelyanskiy, V. N. & Silverstein, M. Fluctuational phase-flip transitions in parametrically driven oscillators. *Phys. Rev. E* **57**, 5202–5212 (1998).
31. Wustmann, W. & Shumeiko, V. Parametric resonance in tunable superconducting cavities. *Phys. Rev. B* **87**, 184501 (2013).
32. Siddiqi, I. et al. Direct observation of dynamical bifurcation between two driven oscillation states of a Josephson junction. *Phys. Rev. Lett.* **94**, 027005 (2005).
33. Wilson, C. M. et al. Photon generation in an electromagnetic cavity with a time-dependent boundary. *Phys. Rev. Lett.* **105**, 233907 (2010).
34. Zhang, Y. & Dykman, M. I. Preparing quasienergy states on demand: a parametric oscillator. *Phys. Rev. A* **95**, 053841 (2017).
35. Wang, Z. et al. Quantum dynamics of a few-photon parametric oscillator. *Phys. Rev. X* **9**, 021049 (2019).
36. Zurek, W. H. Decoherence, einselection, and the quantum origins of the classical. *Rev. Mod. Phys.* **75**, 715–775 (2003).
37. Munro, W. J., Nemoto, K., Milburn, G. J. & Braunstein, S. L. Weak-force detection with superposed coherent states. *Phys. Rev. A* **66**, 023819 (2002).
38. Dykman, M. I., Bruder, C., Lörch, N. & Zhang, Y. Interaction-induced time-symmetry breaking in driven quantum oscillators. *Phys. Rev. B* **98**, 195444 (2018).
39. Puri, S., Andersen, C. K., Grimsmo, A. L. & Blais, A. Quantum annealing with all-to-all connected nonlinear oscillators. *Nat. Commun.* **8**, 15785 (2017).
40. Goto, H. Bifurcation-based adiabatic quantum computation with a nonlinear oscillator network. *Sci. Rep.* **6**, 21686 (2016).
41. Marandi, A., Wang, Z., Takata, K., Byer, R. L. & Yamamoto, Y. Network of time-multiplexed optical parametric oscillators as a coherent Ising machine. *Nat. Photon.* **8**, 937–942 (2014).

Publisher's note Springer Nature remains neutral with regard to jurisdictional claims in published maps and institutional affiliations.

© The Author(s), under exclusive licence to Springer Nature Limited 2020

Experimental implementation

As described in the main text, our experimental implementation consists of a superconducting nonlinear resonator placed inside a 3D microwave cavity (Fig. 1d, Supplementary Information section VI). The main differences with respect to a 3D transmon qubit are as follows. Large capacitor pads help reduce the Kerr nonlinearity of the resonator relative to a transmon and thus limit the drive strength ϵ_2 necessary to reach appreciable coherent-state amplitudes. We orient the resonator such that its dipole moment is perpendicular to the electric field direction of the lowest-frequency cavity mode ($\omega_c/2\pi = 8.9$ GHz) to avoid strong hybridization despite the large pads, and reintroduce a small precisely tuned coupling necessary for dispersive readout by slightly offsetting the pads (note δ in Fig. 1e). Furthermore, instead of a single Josephson junction, we employ a SNAIL²² (Fig. 1f). This makes the resonator flux tunable and endows it with both third- and fourth-order nonlinearities. We use the former to generate single-mode squeezing by applying a coherent microwave drive ω_s at twice the resonator frequency, thus converting one drive photon into two resonator photons through three-wave mixing; the latter yields the required Kerr nonlinearity. An in-depth description of the device design and a full list of system parameters are given in Supplementary Information sections VI, VII, Supplementary Table 2.

Adiabatic mapping between the FQ and KCQ Bloch spheres

Without the large- α approximation from the main text, the expressions for the even and odd cat states are given by $|C_\alpha^\pm\rangle = \mathcal{N}_\alpha^\pm(|+\alpha\rangle \pm |-\alpha\rangle)$, where $\alpha = \sqrt{\epsilon_2/K}$ is the amplitude of the coherent states in the superposition and $\mathcal{N}_\alpha^\pm = 1/\sqrt{2(1 \pm e^{-2\hbar})}$ is a normalization coefficient accounting for $\langle +\alpha | -\alpha \rangle = e^{-2\hbar} \neq 0$ (ref. ⁴, Supplementary Information). These expressions are valid for all ϵ_2/K and, in the limit $\epsilon_2/K \rightarrow 0$, they become $|C_\alpha^+\rangle \rightarrow |n=0\rangle$ and $|C_\alpha^-\rangle \rightarrow |n=1\rangle$. This validates the mapping between the FQ and KCQ Bloch spheres, which share a common definition $|\pm Z\rangle = |C_\alpha^\pm\rangle$ for their respective values of α . We perform the mapping by ramping the squeezing drive on and off with a hyperbolic-tangent profile over 320 ns. To avoid leakage to higher excited states, this time is chosen to be much longer than $1/2K$, where $2K$ corresponds to the anharmonicity of the FQ.

Numerical simulation

Here we describe the numerical simulation performed to obtain the results shown in Fig. 2. For the data presented in Figs. 3, 4 we compensate for all drive-related detunings by calibrating the drive frequencies (Supplementary Information section VIII, Supplementary Fig. 5). However, when measuring the data shown in Fig. 2, it would be impractical to perform this calibration for each drive strength ϵ_2 . Instead we apply the tone generating the squeezing drive at twice the unshifted mode frequency $\omega_s = 2\omega_a$ and the X-rotation drive a frequency $\omega_X/2$. The resulting system Hamiltonian is

$$\hat{H}_s/\hbar = -K\hat{a}^{\dagger 2}\hat{a}^2 + 3g_3\xi(\hat{a}^{\dagger 2} + \hat{a}^2) - 4K|\xi|^2\hat{a}^\dagger\hat{a} + \epsilon_x\hat{a}^\dagger + \epsilon_x^*\hat{a},$$

where we have expressed ϵ_2 in terms of the independently calibrated third-order nonlinearity $g_3 \approx 20$ MHz and the dimensionless drive strength ξ (Supplementary Information section II). The third term corresponds to a drive-dependent frequency detuning due to the a.c. Stark shift.

We perform a numerical simulation of our system, which is described by the master equation

$$\dot{\hat{\rho}} = -\frac{i}{\hbar}[\hat{H}_s, \hat{\rho}] + \kappa_a(1 + n_{\text{th}})\mathcal{D}[\hat{a}]\hat{\rho} + \kappa_a n_{\text{th}}\mathcal{D}[\hat{a}^\dagger]\hat{\rho},$$

here $\mathcal{D}[\hat{O}]\hat{\rho} = \hat{O}\hat{\rho}\hat{O}^\dagger - \frac{1}{2}\hat{O}^\dagger\hat{O}\hat{\rho} - \frac{1}{2}\hat{\rho}\hat{O}^\dagger\hat{O}$, $\hat{\rho}$ is the simulated density matrix of the nonlinear resonator, the dot indicates the time

derivative, $\kappa_a = 1/T_1$ is the single-photon-loss rate of the nonlinear resonator and $n_{\text{th}} = 0.04$ its equilibrium thermal $|1\rangle$ -state occupation number. Our simulation mimics the experiment using the same rise times for the tanh ramps of the squeezing drive (320 ns) and the X-rotation drive (80 ns) up to the point just before mapping back onto the FQ marked by a black arrow in Fig. 2a. At this point, we compute $\langle C_\alpha^\dagger \hat{\rho} | C_\alpha^\dagger \rangle$.

We calibrate the abscissa of Fig. 2b by fitting this simulation to the Rabi frequency obtained at the maximum strength of the squeezing drive using the corresponding value of ξ (or equivalently ϵ_2) as the only free parameter. We then perform the simulation for all other values of ϵ_2 to obtain the solid black line shown in the figure. The black line in the bottom panel of Fig. 2d corresponds to the result of one of these simulations (marked by a red star in Fig. 2b) scaled to match the contrast of the data. This accounts for the fact that in the experiment the state $|C_\alpha^\pm\rangle$ is mapped onto the $|0\rangle$ state of the FQ, which is then measured. This process as well as the finite mapping and measurement fidelities are not part of the simulation. The black lines in the other two panels of this figure are obtained by changing $\arg(\epsilon_x)$ but using same scaling factor.

Experimental details of the gate process tomography

Here we describe pulse sequences used to obtain the data presented in Fig. 3a, c, e. At the beginning of each sequence, the FQ is initialized in one of the six states $|\pm X\rangle, |\pm Y\rangle$ and $|\pm Z\rangle$. These are then adiabatically mapped onto the KCQ. Each sequence ends with the reverse mapping and measurement of the resulting $\langle X \rangle, \langle Y \rangle$ and $\langle Z \rangle$ component of the FQ state using appropriate FQ pulses (grey box in the figures).

To perform the $X(\pi/2)$ gate, we apply a Gaussian pulse with a duration of 24 ns and a maximum amplitude of $\epsilon_{X, \pi/2} = 6.5$ MHz.

To implement a $Z(\pi/2)$ gate, we abruptly set the squeezing drive amplitude to zero for a duration $T_{Z(\pi/2)} = 38$ ns and then switch it on again, as shown in Fig. 3e. Our room-temperature electronics limit the rise and fall times of ϵ_2 to about 4 ns with a maximum time resolution of 2 ns.

Experimental details of the CR

During the CR, we perform heterodyne detection of the emitted cavity field. The data in Fig. 4a are a histogram of 3×10^5 measurements of this demodulated and integrated field.

We conservatively define the total readout fidelity as $\mathcal{F} = 1 - p(-\alpha | +\alpha) - p(+\alpha | -\alpha) = 0.74$, where $p(-\alpha | +\alpha) = 0.13$ ($p(+\alpha | -\alpha) = 0.13$) is the probability of measuring the qubit in $|-\alpha\rangle$ ($|+\alpha\rangle$) after initialization in $|+\alpha\rangle$ ($|-\alpha\rangle$).

We characterize the quantum-non-demolition aspect by evaluating $\mathcal{Q} = (P(+\alpha | +\alpha) + P(-\alpha | -\alpha))/2 = 0.85$, where $P(i | i)$ is the probability of obtaining the measurement outcome i in two successive measurements (Supplementary Information section IX, Supplementary Fig. 6).

Supplementary information content

The accompanying Supplementary Information contains further details on: the general encoding (section I), the full system Hamiltonian (section II), direct spectroscopy of the energy gap (section III, Supplementary Fig. 1), the continuous X rotation (section IV), the characterization of the gate operations (section V, Supplementary Figs. 2, 3, Supplementary Table 1), the experimental setup (section VI, including a detailed wiring diagram in Supplementary Fig. 4), the system parameters (section VII, including a summary Supplementary Table 2), the experimental tune-up sequence (section VIII, Supplementary Fig. 5), the CR (section IX, Supplementary Fig. 6), the measurement of the KCQ coherence times obtained by mapping back onto the FQ and performing dispersive readout (section X, Supplementary Fig. 7) and a discussion of the impact of different

decoherence processes on the KCQ (section XI, Supplementary Fig. 7).

Data availability

The data that support the findings of this study are available from the corresponding authors upon reasonable request.

Code availability

Numerical simulations were performed using a Python-based open source software (QuTiP). Custom Python code was used to obtain and analyse the experimental data following standard practices as outlined in Methods and the Supplementary Information. The code used in this study is available from the corresponding authors upon reasonable request.

Acknowledgements We acknowledge the contributions of L. Burkhardt, P. Campagne-Ibarcq, A. Eickbusch, L. Frunzio, P. Reinhold, K. Serniak and Y. Zhang. Facilities use was supported by YINQE and the Yale SEAS cleanroom. This work was supported by ARO under grant number W911NF-18-1-0212 and grant number W911NF-16-1-0349, and NSF under grant number DMR-1609326. We also acknowledge support of the Yale Quantum Institute.

Author contributions A.G. designed and carried out initial experiments with help from S.T. and S.O.M., and designed the final experiment with input from N.E.F., M.H.D. and S.P. A.G. and N.E.F. fabricated the sample, performed measurements and analysed the data used in the manuscript. A.G., N.E.F. and M.H.D. wrote the manuscript with input from all authors.

Competing interests M.H.D. is a co-founder of Quantum Circuits, Incorporated. A.G., S.P., S.M.G. and M.H.D. are inventors on US Provisional Patent Application Number 62/692,243 submitted by Yale University, which covers quantum information processing with an asymmetric error channel.

Additional information

Supplementary information is available for this paper at <https://doi.org/10.1038/s41586-020-2587-z>.

Correspondence and requests for materials should be addressed to A.G. or M.H.D.

Reprints and permissions information is available at <http://www.nature.com/reprints>.